



Impact of the Gulf Stream front on atmospheric rivers and Rossby wave train in the North Atlantic

Xiaohui Ma^{1,2} · Yinglai Jia³ · Ziqing Han³

Received: 17 July 2023 / Accepted: 26 February 2024
© The Author(s) 2024

Abstract

The Gulf Stream (GS) ocean front exhibits intense ocean–atmosphere interaction in winter, which has a significant impact on the genesis and development of extratropical cyclones in the North Atlantic. The atmospheric rivers (ARs), closely related with the cyclones, transport substantial moisture from the North Atlantic towards the Western European coast. While the influence of the GS front on extratropical cyclones has been extensively studied, its effect on ARs remains unclear. In this study, two sets of ensemble experiments are conducted using a high-resolution global Community Atmosphere Model forced with or without the GS sea surface temperature front. Our findings reveal that the inclusion of the GS front leads to approximately 25% enhancement of water vapor transport and precipitation associated with ARs in the GS region, attributed to changes in both AR frequency and intensity. Furthermore, this leads to a more pronounced downstream response in Western Europe, characterized by up to 60% (40%) precipitation increases (reductions) around Spain (Norway) for the most extreme events (exceeding 90 mm/day). The influence of the GS front on ARs is mediated by both thermodynamic and dynamic factors. The thermodynamic aspect involves an overall increase of water vapor in both the GS region and Western Europe, promoting AR genesis. The dynamic aspect encompasses changes in storm tracks and Rossby wave train, contributing to downstream AR shift. Importantly, we find the co-occurrence of ARs and the GS front is crucial for inducing deep ascending motion and heating above the GS front, which perturbs the deep troposphere and triggers upper-level Rossby wave response. These findings provide a further understanding of the complex interaction between the oceanic front in the western boundary current regions and extratropical weather systems and the associated dynamics behind them.

Keywords Gulf Stream front · Atmospheric rivers · Extratropical cyclones · Rossby wave train

1 Introduction

The Gulf Stream (GS) and its extension transport large amounts of heat and moisture into the extra-tropics, particularly during the winter season, resulting in intense ocean–atmosphere interactions in the North Atlantic. The coupling between the oceanic front and mesoscale eddies with the atmosphere as well as their impact on the extratropical weather systems in the western boundary current

regions including the GS, Kuroshio extension, and Agulhas current regions have been extensively examined (see Small et al. 2008; Czaja et al. 2019; Seo et al. 2023 for reviews). Previous studies have revealed the influence of the GS front on extratropical storms through its modification of sea surface temperature (SST) gradients, moist and diabatic heating processes (Kuwano-Yoshida and Minobe 2017; Small et al. 2018; Bui and Spengler 2021; Tsopouridis et al. 2021). The presence of the GS front has been found to affect the low-level baroclinicity, modifying the storm track and shifting it poleward or equatorward in the North Atlantic (Graff and LaCasce 2012; Piazza et al. 2016; Lee et al. 2018; Czaja et al. 2019; Foussard et al. 2019). Moreover, the warm sector of the GS front supports intensified ascending motion within the warm conveyor belt of extratropical cyclones, facilitating the growth of cyclones (Sheldon et al. 2017). Recently, Parfitt et al. (2016) proposed the “thermal damping and strengthening” (TDS) theory to explain the interaction

✉ Yinglai Jia
jjayingl@ouc.edu.cn

¹ Key Laboratory of Physical Oceanography and Frontiers Science Center for Deep Ocean Multispheres and Earth System, Ocean University of China, Qingdao, China

² Laoshan Laboratory, Qingdao, China

³ College of Oceanic and Atmospheric Sciences, Ocean University of China, Qingdao, China

between the atmospheric front and the underlying oceanic front. All these studies underline the critical role of frontal and mesoscale SST forcing associated with the GS front in affecting synoptic-scale atmospheric weather systems in the mid-latitude.

The airflow within the warm sector of an extratropical cyclone can transport moisture into the cyclone and form a high moisture flux convergence band known as atmospheric rivers (ARs) (Dacre et al. 2015). ARs can induce extreme rain and flooding events when they make landfall in coastal regions like the west coast of North America in the North Pacific and Western Europe in the North Atlantic (Lavers and Villarini 2013; Guan and Waliser 2015). Despite extensive discussions on the interaction between mesoscale SSTs and extratropical cyclones, studies exploring the potential impacts of frontal and mesoscale SSTs on ARs are only beginning to emerge. A recent work by Liu et al. (2021) revealed the remote forcing effect of the Kuroshio front and eddies on ARs and heavy precipitation along the west coast of North America. They demonstrated that the presence of ocean front and eddies can enhance AR and AR-induced precipitation by up to 30%. The asymmetric atmospheric responses to warm and cold eddies result in net moisture transport above the planetary boundary layer (PBL) and the moisture entering above the PBL interacts with upper level higher momentum within the extratropical cyclones, favorable for AR genesis and subsequent downstream water vapor transport. Other studies have also shown that the GS front can increase moisture availability and affect the frequency and intensity of landfalling ARs over Western Europe (Wu et al. 2020; Zavadoff and Kirtman 2020; McClenny et al. 2020). These studies highlight the importance of oceanic front and eddies in modifying the moisture supply in ARs, primarily through potential thermodynamic responses to mesoscale SSTs. Given that the formation of ARs involves the transport of high water vapor, which is influenced by both moisture and wind fields, it is crucial to explore potential dynamic modifications of mesoscale SSTs on ARs.

As ARs exhibit a close relationship with extratropical storms (Zhang et al. 2019a), it is plausible that changes in storm tracks induced by mesoscale SSTs have a dynamic impact on ARs. Existing studies suggest that the presence of oceanic fronts and eddies in the western boundary current regions tends to enhance storm intensity and modify its downstream development (Ma et al. 2017; Kuwano-Yoshida and Minobe 2017; Foussard et al. 2019; Zhang et al. 2019b). These changes in the storm track, in turn, may potentially influence ARs through alterations in the wind field. However, it is important to note that although ARs and storm responses may be highly related, they are not necessarily synonymous, as only 40% of extratropical storms are associated with ARs (Zhang et al. 2019a). Thus, a comprehensive

understanding of the dynamical AR response related to storm tracks requires further investigation.

An additional possible dynamic process that connects mesoscale SSTs and ARs is Rossby wave propagation. Recent studies have revealed that intense diabatic heating associated with ARs can perturb the upper-level atmosphere, leading to Rossby wave breaking events and wavelike pattern responses (Piazza et al. 2016; Zavadoff and Kirtman 2020; Hsu and Chen 2020; de Vries 2021). The propagation of Rossby wave will further regulate the paths of ARs and extratropical storms. Although it has been shown that the presence of oceanic front and eddies will modify the diabatic heating release (Ma et al. 2017; Foussard et al. 2019), the direct linkage between mesoscale oceanic processes and Rossby wave response, as well as the implications of these wave changes on ARs, remain unresolved.

In this paper, we aim to study the impact of the GS front on ARs in the North Atlantic, utilizing a high resolution global model—the 5th version of Community Atmosphere Model (CAM5). A common approach employed in studying the influence of oceanic fronts is to compare atmospheric simulations forced with original and smoothed SST (Piazza et al. 2016; O'Reilly et al. 2017; Tsopouridis et al. 2021). Following previous studies, two sets of parallel experiments forced with and without the GS front are conducted. The structure of the paper is organized as follows. In Sect. 2, the experiment design, data and methods are introduced. Section 3 presents the main results, including model validations, the effects of the GS front on ARs and Rossby wave trains, and the thermodynamic and dynamic processes involved. Section 4 gives the conclusions and discussions.

2 Experiments and methods

2.1 High resolution global model experiments

The global climate model utilized in this study is CAM5 with a spectral element dynamic core, conducted at a horizontal resolution of approximately 0.25° . According to previous studies (Willison et al. 2013; Ma et al. 2015, 2017), the 0.25° resolution is sufficient to resolve the mesoscale SSTs and atmosphere coupling. The model uses prescribed SST and sea ice derived from daily 0.25° NOAA Optimum Interpolation SST and ICE (OISST). The simulations contain 13 boreal winter (DJF) twin experiments from 2000 to 2013, referred to as control (CTRL) and filtered (FLTR). Each twin simulation consists of 5 ensemble members, initialized on December 1 with slightly perturbed initial states, and integrated for a period of 3 months. The initial 15-day period of each run was discarded to eliminate the spin-up of the model.

In CTRL, the high-resolution satellite SST was applied and the sharp SST front in the GS region was retained. In FLTR, a $4^\circ \times 4^\circ$ boxcar low-pass filter was applied to SST field in the GS region (81.25°W – 20°W , 25°N – 57°N , outlined by the grey box in Fig. 1). The width of the filter window was chosen based on the typical length scale of mesoscale SSTs in the region. To ensure a smooth transition between the filtered region and its surroundings, an 11-grid smoothing was applied along the boundary of the filtered zones. Figure 1 illustrates the winter season mean SST difference between the CTRL and FLTR. A dipole pattern of SST anomalies aligning with the GS front is removed in FLTR (Fig. 1a), leading to a reduction in SST gradient along the GS. The largest SST signal removed corresponds to the area of intense ocean-atmospheric coupling, as demonstrated by previous studies (e.g., the strong wind convergence and precipitation above the GS front as reported in Kwon et al. 2010; Minobe et al. 2008, 2010). Furthermore, the application of SST smoothing results in a 30–50% decrease in the SST standard deviation along the GS path (Fig. 1b–d), corresponding to the weakening of the GS variability, which largely reflects the reduced mesoscale oceanic eddy activities in FLTR (Fig. 1b–d).

2.2 AR detection

ARs are identified by searching for long narrow integrated water vapor transport (IVT) anomalies (subtracted by the climatological winter season mean) that exceed $250 \text{ kg m}^{-1} \text{ s}^{-1}$ (Zhu and Newell 1998; Gimeno et al. 2014) based on daily IVT data. The outer edge of an AR is defined by a closed IVT contour of $250 \text{ kg m}^{-1} \text{ s}^{-1}$. For an event to be classified as an AR, it must have a length greater than 2000 km and a width narrower than 1000 km. The center of an AR is determined as the geometric center of the IVT contour. The AR-related precipitation is defined as the precipitation that falls within the closed IVT contour of an AR (Guan and Waliser 2015). In total, 3555 (3494) ARs are detected in the 65 ensemble winters in CTRL (FLTR), corresponding to approximately 55 ARs per winter. To assess the model's performance, ERA5 reanalysis data covering the same time period (2000–2013) are analyzed. 674 ARs are identified in the North Atlantic region during the selected period in ERA5, corresponding to an average of 52 ARs per winter, which is comparable with the model results.

To explore the atmospheric responses associated with individual ARs, composite analyses of ARs' structure are conducted from a Lagrangian perspective (Fig. 6). Specifically, all ARs are aligned at the same location by fixing their AR centers. Variables within a specified radius

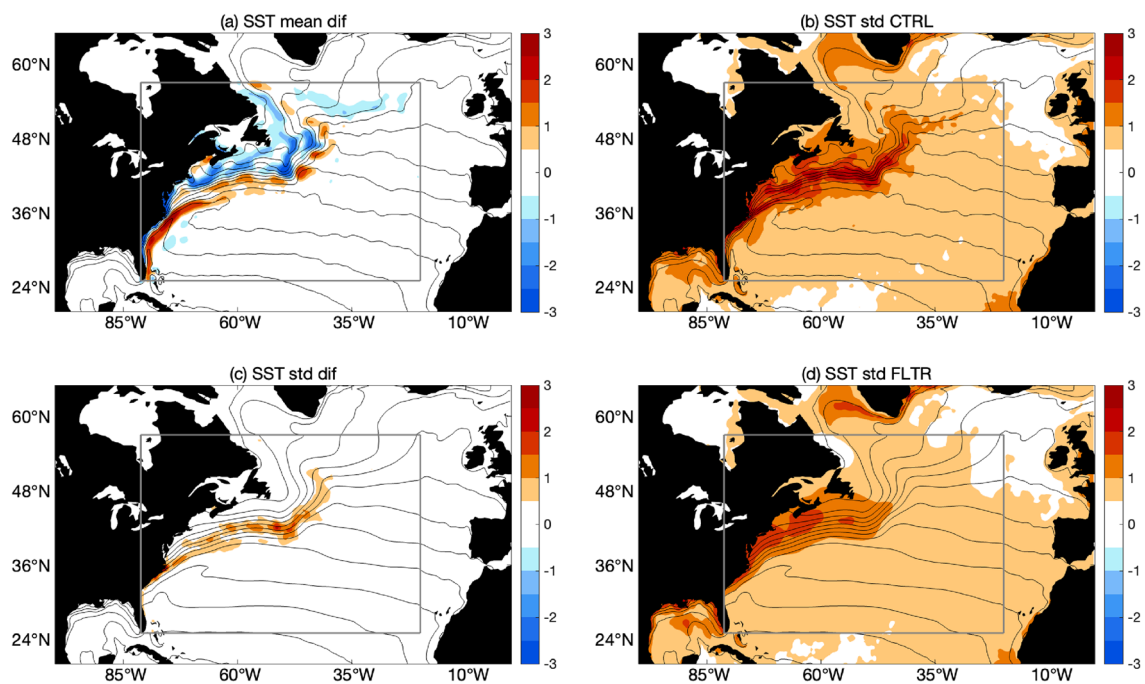


Fig. 1 SST forcing in CTRL and FLTR simulations. **a** The winter season mean SST ($^\circ\text{C}$, from 0 to 30°C with interval 2°C) in CTRL (contours) and the difference between CTRL and FLTR (shaded). Standard deviation of SST forcing in CTRL (**b**) and FLTR (**d**). The

difference of standard deviation between CTRL and FLTR (**c**). Black contours in (**a**, **b**) represent winter mean SST in CTRL and those in (**c**, **d**) are for FLTR. The SST smoothing is applied in the grey box ($[81.25^\circ \text{W}$ – 20°W , 25°N – $57^\circ \text{N}]$)

around the AR center, referred to as one AR radius (1R), are selected and normalized by the AR radius. Subsequently, an AR composite is constructed by averaging all the normalized variables together. This composite analysis presents the detailed atmospheric structure associated with ARs.

To investigate the atmospheric responses to the GS front in the presence and absence of ARs, separate composite analyses for AR days and non-AR days are performed from an Euler perspective (Figs. 8, 9, 11). The AR days are defined as those when ARs pass the GS region (30° N–47.5° N, 80° W–45° W) and over 50% of the AR grids lie within the chosen region while the remaining days are classified as non-AR days.

2.3 Apparent heat source and wave activity flux

We did not enable the direct output of diabatic heating in our CAM model. To estimate diabatic heating in this study, we calculated the apparent heat source according to the following equation (Yanai et al. 1973):

$$Q1 = \left(\frac{p}{p_0}\right)^{R/C_p} \left(\frac{\partial\theta}{\partial t} + \mathbf{v} \cdot \nabla\theta + \omega \frac{\partial\theta}{\partial p}\right) \quad (1)$$

In Eq. (1), θ is the potential temperature, $\mathbf{v} = (u, v)$ is the horizontal wind velocity, ω is the vertical p -velocity, and p is the pressure. R and C_p are, the gas constant and the specific heat at constant pressure of dry air, respectively. p_0 is 1000 hPa, ∇ is the isobaric gradient operator.

The wave activity flux is a useful diagnostic tool for studying the propagating of stationary wave packet and is calculated using the following equation according to Takaya and Nakamura (2001):

$$W = \frac{1}{|\bar{\mathbf{v}}|} \left(\begin{array}{c} \bar{u}(\psi_x'^2 - \psi' \psi_{xx}') + \bar{v}(\psi_x' \psi_y' - \psi' \psi_{xy}') \\ \bar{u}(\psi_x' \psi_y' - \psi' \psi_{xy}') + \bar{v}(\psi_y'^2 - \psi' \psi_{yy}') \\ \frac{f^2}{R\sigma/p} \left\{ \bar{u}(\psi_x' \psi_p' - \psi' \psi_{xp}') + \bar{v}(\psi_y' \psi_p' - \psi' \psi_{yp}') \right\} \end{array} \right) \begin{array}{c} \bar{i} \\ \bar{j} \\ \bar{k} \end{array} \quad (2)$$

where ψ is the stream function, f the Coriolis parameter, R the gas constant, $\mathbf{v} = (u, v)$ the horizontal wind velocity, $\sigma = \left(\frac{RT}{C_p p}\right) - dT/dp$, with temperature T and the specific heat at constant pressure C_p . Overbars represent the temporal average (winter season mean) and the primes are the anomalies from the time mean. The divergence of wave activity flux indicates the “wave source” region where waves get the available potential energy from the mean flow (Takaya and Nakamura 2001).

3 Results

3.1 Model validations

The model’s capability in reproducing AR, IVT and precipitation is first evaluated by comparing simulated fields with ERA5 reanalysis (Fig. 2). In ERA5, the winter season mean IVT show an IVT maxima along the southern flank of the GS front and a northeastward extension, collocating with the warm GS front (Fig. 2a). The high precipitation is also confined along the southern edge of the GS front, but with narrower spread compared with IVT (Fig. 2b). Heavy precipitation is observed further downstream along the coasts of Western Europe, probably due to the topography lifting (Fig. 2b; Lavers and Villarini 2013; Guan and Waliser 2015). The pronounced IVT above the warm oceanic front corresponds to a high occurrence frequency of ARs south of the GS front (Fig. 2c), reaching a maximum frequency of $\sim 12\%$ throughout the winter season. The spatial distribution of AR-related precipitation closely follows that of AR occurrence frequency and its contribution to the total precipitation is approximately 20% in the GS region (Fig. 2d), consistent with previous findings (Guan and Waliser 2015; Arabzadeh et al. 2020).

In comparison, CAM CTRL simulations reproduce the spatial distribution and strength of total IVT and precipitation, ARs and AR-related precipitation reasonably well (Fig. 2e–h). Particularly, the model successfully captures the topography-induced precipitation along the western European coasts, affirming the model’s capability to simulate both the background and AR-related IVT and precipitation. However, it is worthwhile to point out that the occurrence frequency of ARs and the amplitude of AR-related precipitation simulated in CAM are slightly overestimated (Fig. 2g, h). However, this model-induced overestimation is consistent in both CTRL and FLTR simulations, thereby limiting its impact on the subsequent analyses that focus on the differences between CTRL and FLTR.

3.2 Impacts of the GS front on ARs

The AR and AR-related precipitation responses to the smoothing of the GS front are shown in Fig. 3. The presence of the GS front in CTRL results in $\sim 20\%$ strengthening of AR occurrence and $\sim 15\%$ increase in AR mean IVT intensity localized along the GS front (Fig. 3a, b), collocating with the largest mesoscale SST signal removed. Correspondingly, the accumulated AR IVT and precipitation in CTRL are enhanced by approximately 25% along the southern flank of the GS front (Fig. 3c, d). Note that the

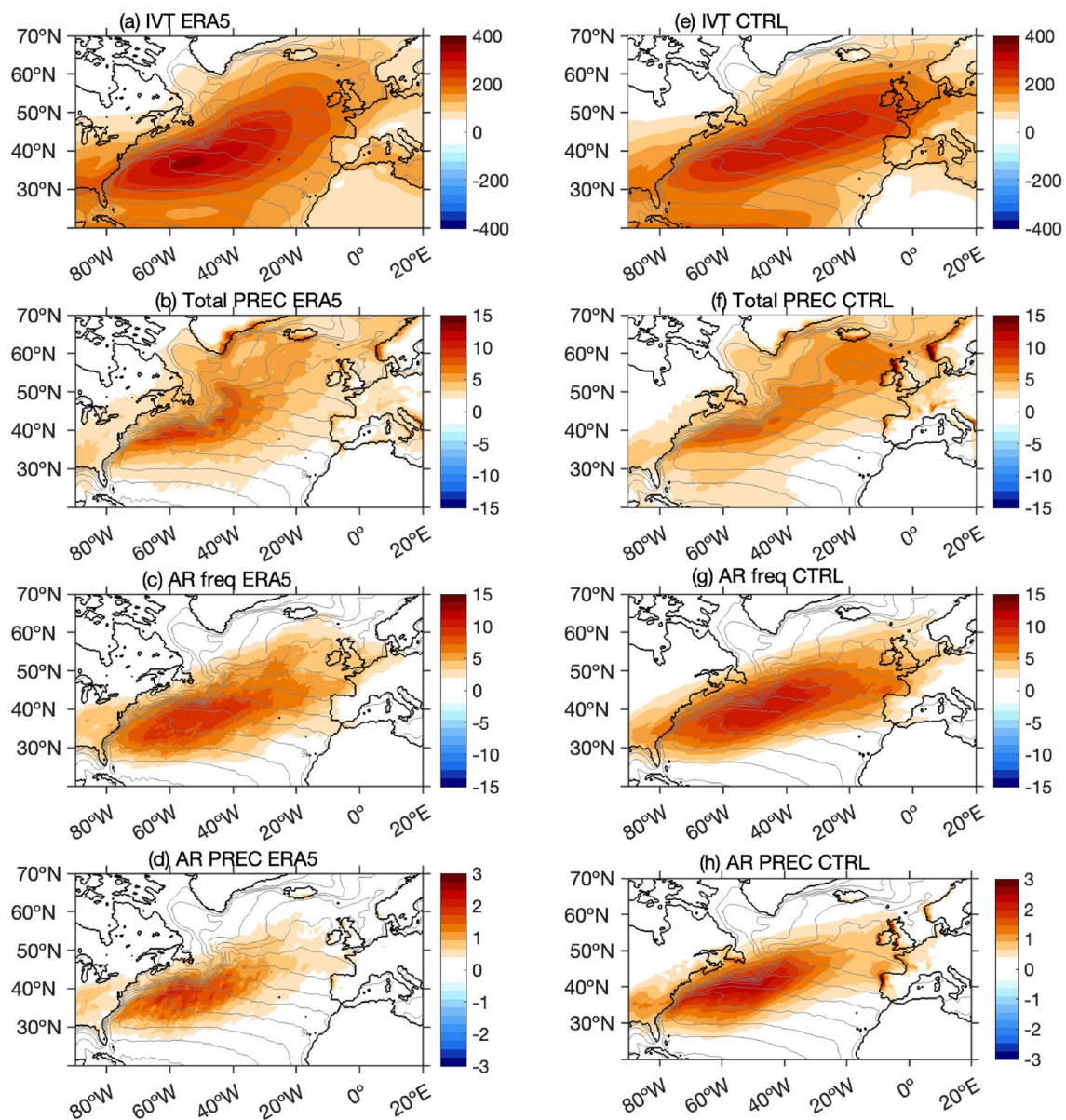


Fig. 2 Winter season mean IVT (shading, kg m⁻¹ s⁻¹) (a), total precipitation (shading, mm day⁻¹) (b), AR occurrence frequency (shading, %) (c) and AR related accumulated precipitation (shading,

mm day⁻¹) (d) in ERA5. (e–h) same as (a–d), but for CAM CTRL simulations. The grey contours in (a–d) are winter season mean SST in ERA5 while those in (e–h) are SST for CTRL

accumulated AR IVT increase here represents a combined impact of changes in both AR frequency and intensity. The enhanced AR activity in the GS region is consistent with previous studies on the atmospheric response to mesoscale SSTs, which have reported increased water vapor, precipitation, and intensified storm growth in response to oceanic fronts and eddies within western boundary current regions (Liu et al. 2021; Sheldon et al. 2017; Sugimoto et al. 2017). In this study, similar water vapor increase and cyclone intensification associated with the warm GS front that contributed to the enhanced AR are observed

and verified in the following analyses (Figs. 6, 7). We also noted a significant increase of AR-related precipitation north of the GS front near Gulf of St Lawrence, probably related with ARs making landfall on the northeastern coast of North America, as revealed in previous studies (Hsu and Chen 2020).

In addition to the local AR response within the GS region, a pronounced downstream response with a distinct southward shift of ARs along the coast of Western Europe is observed (Fig. 3a–d). In CTRL, the presence of the GS front leads to a reduction (enhancement) in AR occurrence

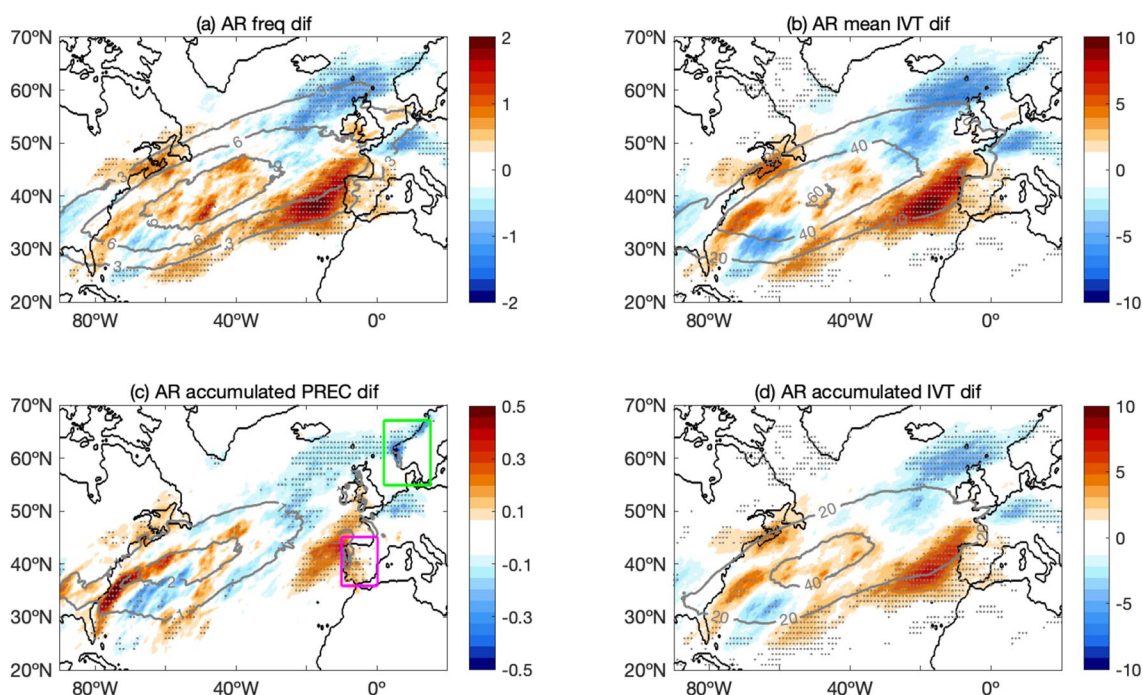


Fig. 3 The difference of AR occurrence frequency (shading, %) (a), AR mean IVT (shading, $\text{kg m}^{-1} \text{s}^{-1}$) (b), AR accumulated precipitation (shading, mm day^{-1}) (c), and AR accumulated IVT (shading, $\text{kg m}^{-1} \text{s}^{-1}$) (d) between CTRL and FLTR. Grey contours are the corresponding values in CTRL. At each grid, the AR mean IVT is computed as the sum of AR IVT divided by the total number of ARs, while the AR accumulated IVT is computed as the sum of AR IVT

north (south) of 50°N in Western Europe (Fig. 3a). This shift pattern is further reflected in the AR-IVT and AR-related precipitation, with amplified precipitation response observed in the high topographical areas along the coast of Western Europe (Fig. 3c). Although the occurrence of ARs only accounts for approximately 10% of the total winter season days, the contribution of AR-related precipitation to total precipitation can reach as high as 80% when daily precipitation exceeds 80 mm/day (Fig. 4a, b, d, e). Furthermore, the remote response to ARs is even stronger than the local response. The reduction in AR-related precipitation near Norway varies from 10 to 40%, with the reduction peaking at 40% for the most extreme events ($> 90 \text{ mm/day}$). In contrast, precipitation increase around Spain ranges from 20 to 60%, with the highest increase reaching up to 60% for extreme events (Fig. 4c, f). These results indicate the significant contribution of ARs to extreme precipitation, with the AR-related extreme precipitation being predominantly influenced by the GS front and further intensified by topographic lifting. Our examination of the background IVT difference between CTRL and FLTR indicates that the influence of the GS front on background IVT (with a 2% increase in the local GS region and a 10% increase downstream in Western Europe) is markedly less pronounced than its impact

divided by the total number of winter season days. The dots represent differences significant above the 95% confidence level based on a two-tailed Student's test. The green and magenta boxes in c outline the northern (55°N – 67°N , 2°E – 15°E) and southern (36°N – 45°N , 10°W – 0°E) regions to calculate the probability density functions (PDF) of rain in Fig. 4

on ARs. Consequently, the contribution of background IVT change to AR response, both locally and remotely, is limited.

It has been noted that the downstream response of ARs is even stronger than the upstream response, despite being away from the GS SST forcing area. To trace the origin of downstream AR response, a lag composite analysis of landfalling ARs along the coast of Western Europe was performed. Here, landfalling ARs are defined as instances where the outmost contour of an AR insect with the coastline of Western Europe. Figure 5 illustrates the evolution of AR occurrence frequency from genesis in the GS region (lag -3) to landfall in Western Europe (day 0) in CTRL and the corresponding differences between CTRL and FLTR. Originating in the GS region, ARs pick up moisture from the warm GS front and gradually intensify (Fig. 5a–c). The subsequent evolution of ARs involves a continuous water replenishment and depletion. Upon landfall, heavy precipitation forms and a large amount of water vapor is released, leading to the gradual decay of ARs (Fig. 5d). On average, it takes approximately 4 days for ARs to propagate from the GS region to Western Europe, corresponding to a propagation speed of approximately 20 m/s , which aligns with the typical travel speed of extratropical storms. The inclusion of the GS front supports higher AR genesis in the GS region

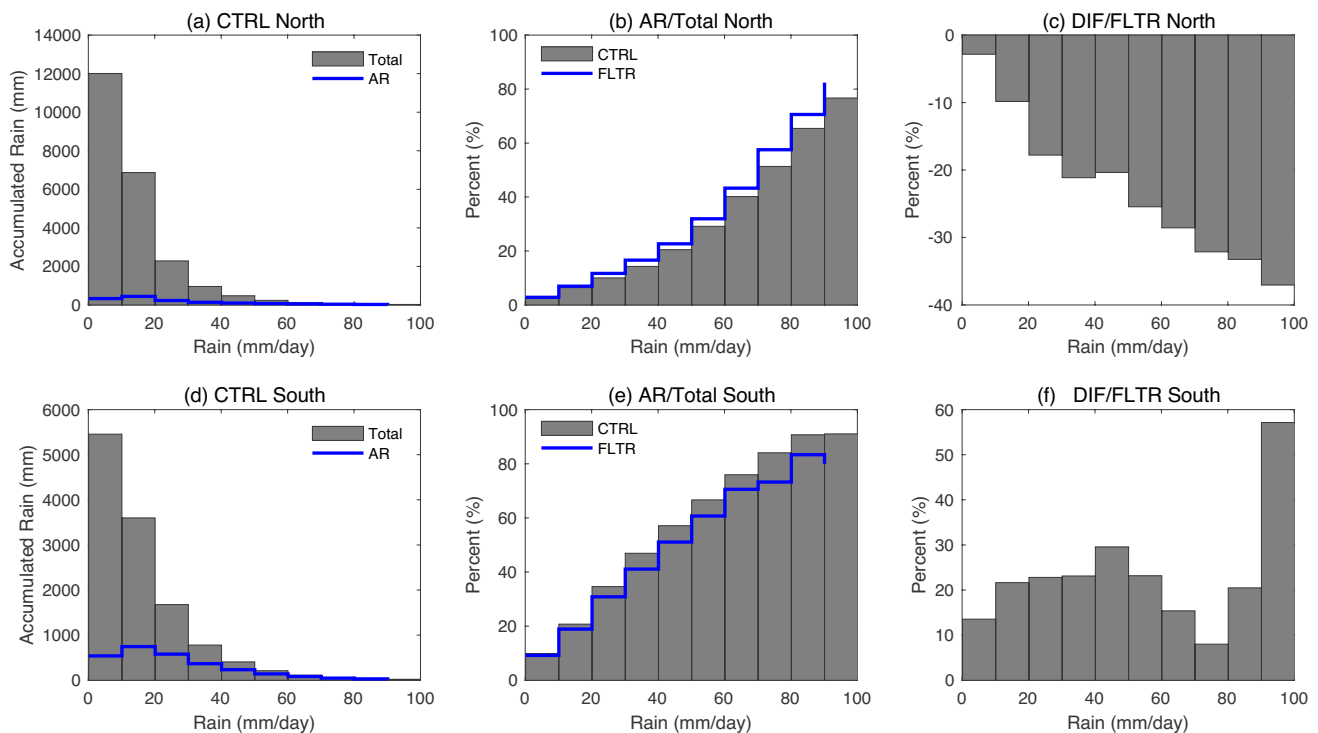


Fig. 4 **a** PDF of total precipitation (histogram) and AR related precipitation (blue line) in the northern box region. **b** PDF of fractional contribution (%) of AR related precipitation to total precipitation in CTRL (histogram) and in FLTR (blue line) in the northern box

region. **c** PDF of fractional difference of AR related precipitation (CTRL-FLTR) in reference to FLTR in the northern box region. **(d–f)** same as **(a–c)**, but for rain PDFs in the southern box region

(Fig. 5e, f), consistent with the local intensification of AR activity shown in above Fig. 3. The downstream propagation of ARs is further influenced by storm tracks and large-scale atmospheric circulations, as discussed in the subsequent section, displaying a shift pattern upon landfall (Fig. 5g, h). The lag composite analysis suggests that, although there are significant differences between the local and remote AR responses, the changes observed downstream can be traced back to the GS region, which is induced by the smoothing of SST applied in this region.

The detailed structural changes of ARs between CTRL and FLTR are examined by conducting the composite analysis of individual ARs following the evolution of ARs (see Sect. 2.2 for details). The composites of ARs in CTRL (Fig. 6) show that an AR is typically accompanied by a dipole of sea level pressure (SLP) anomalies, with a low-pressure cyclone system located northwest of the AR and a high-pressure anticyclone to the southeast (Fig. 6c), consistent with previous studies (Zhang et al. 2019a). High winds form ahead of the cyclone where the pressure gradient is strongest, transporting water vapor into the narrow front of the cyclone known as the warm conveyor belt (Fig. 6a). Recent research by Dacre et al. (2019) revealed that one branch of the water vapor enters the cyclone center and ascends, leading to the release of extensive diabatic heating

that supports cyclone growth. The other branch exports moisture from the cyclone, resulting in a filament of high moisture content and the formation of ARs. As can be seen, the maximum IVT and water vapor locate southeast of the cyclone center and align in a southwest-northeast direction (Fig. 6a, b). Correspondingly, intensive upward motion (W) and diabatic heating (apparent heat source, Q_1) develop within the cyclone and are particularly strong along the warm conveyor belt (Fig. 6d, e).

The presence of the GS front not only modifies the occurrence frequency of ARs but also strengthens their intensity. When the GS front is included in the CTRL simulations, stronger ARs characterized by higher water vapor and IVT are observed compared to FLTR (Fig. 6f, g). The most significant increases in water vapor and IVT occur around the center and along the southern flank of the AR. The amplitude of water vapor and IVT change is approximately 5%, which is relatively low compared to the AR-IVT change shown in Fig. 3. This is because the AR-IVT composite here mainly represents the intensity change of ARs, while the AR-IVT change in Fig. 3 is accumulated that considers both AR intensity and frequency changes. Nevertheless, the composite analysis indicates a significant overall enhancement of AR intensity in CTRL. The enhanced ARs are accompanied by intensified cyclones with deeper SLP

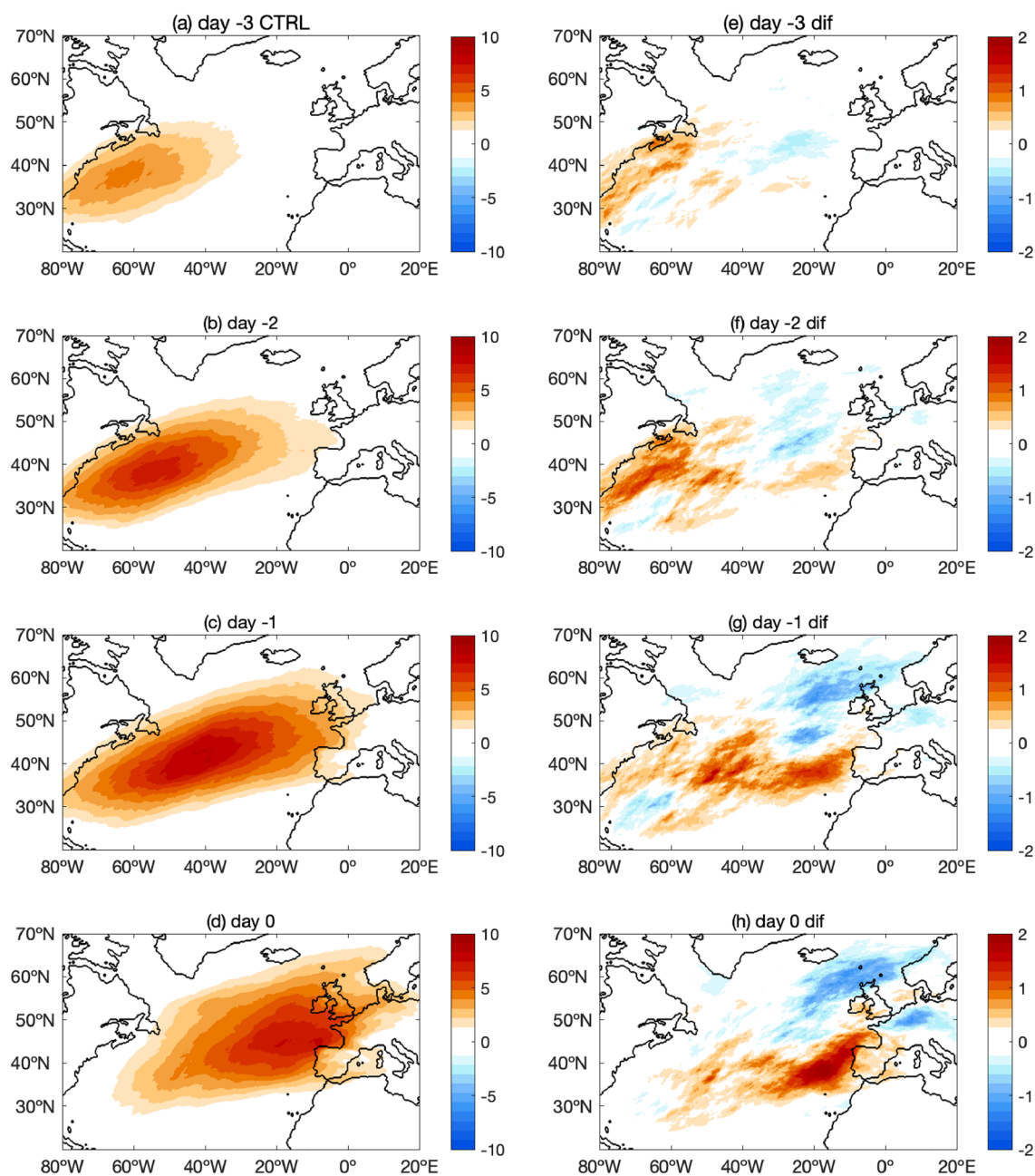


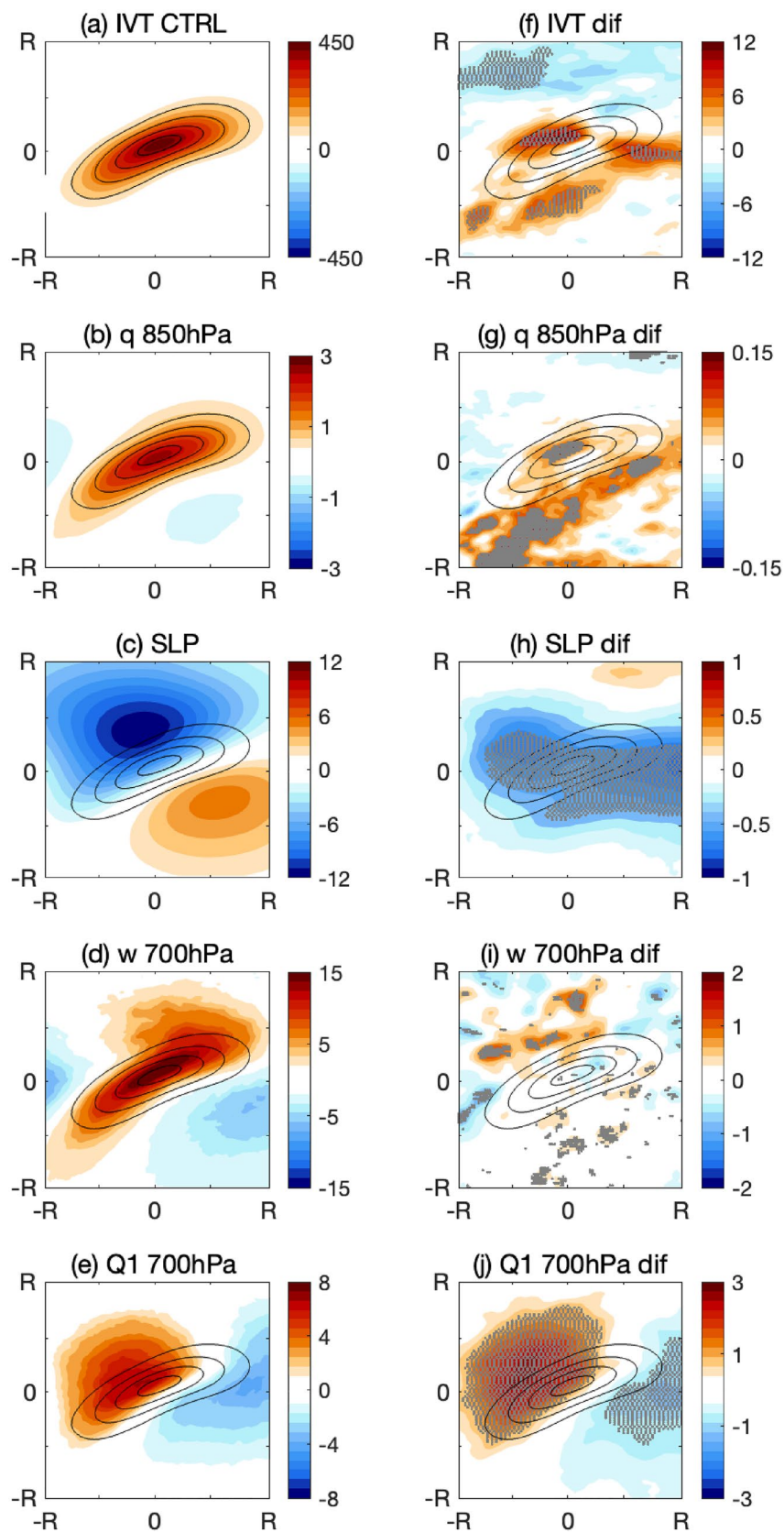
Fig. 5 Composites of AR occurrence frequency (%) by tracing back the development of ARs making landfall along the coast of Western Europe from day -3 (3 days previous to landfalling) to day 0

anomalies (Fig. 6h), consistent with previous studies that have reported increased storm intensity in the presence of oceanic fronts and mesoscale eddies in the Kuroshio region (Ma et al. 2017; Kuwano-Yoshida and Minobe 2017). The stronger cyclone intensity, along with the enhanced water vapor increase, favors more intense AR genesis. A notable difference between CTRL and FLTR ARs is the substantially stronger upward motion (W) and diabatic heating (Q1) observed in CTRL ARs. The 700 hPa Q1 associated with

(landfalling day) in CTRL (a–d), and the corresponding differences between CTRL and FLTR (e–h)

CTRL ARs is approximately 50% greater than that in FLTR (Fig. 6j). It should be noted that, in addition to the modification of water vapor transport by the GS front, which alters AR occurrence frequency and intensity, another important change induced by the GS front is the release of diabatic heating. It is evident that more diabatic heating associated with ARs is released into the atmosphere in the presence of the GS front. This additional diabatic heating may play a significant role in generating upper troposphere and large-scale

Fig. 6 Composites of IVT (shading, $\text{kg m}^{-1} \text{s}^{-1}$) (a), specific humidity at 850 hPa (shading, g kg^{-1}) (b), SLP anomaly (shading, hPa) (c); vertical velocity anomaly at 700 hPa (shading, $-10^{-2} \text{ Pa s}^{-1}$) (d) and Q1 anomaly at 700 hPa (shading, K day^{-1}) (e) associated with ARs in CTRL. (f–j) same as (a–e), but for the corresponding differences between CTRL and FLTR. The black contours in (a–j) outline the position of ARs which is represented by the composite of AR IVT. Differences significant above the 95% confidence level are shaded by grey dots based on a two-tailed Student's test



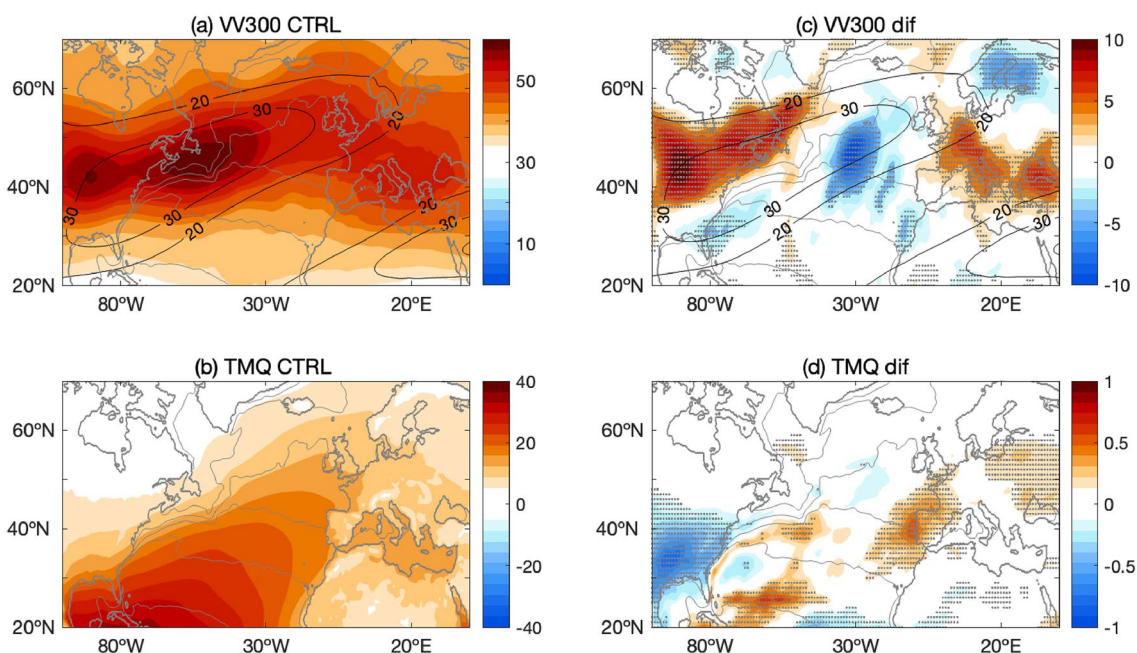


Fig. 7 The winter season mean storm track ($V'V'$, shading, $\text{m}^2 \text{s}^{-2}$) and zonal wind (U , black contours, m s^{-1}) at 300 hPa in CTRL (a) and the difference between CTRL and FLTR (c). V' is derived as 5–12-day Lanczos band-pass filtered meridional wind. The winter season mean column-integrated water vapor (TMQ, shading, kg/m^2)

in CTRL (b) and the difference between CTRL and FLTR (d). The grey contours in a–d are winter mean SST in CTRL. Differences significant above the 95% confidence level are shaded by grey dots based on a two-tailed Student's test

Rosby wave responses in the North Atlantic, which will be discussed in detail in Sect. 3.5.

3.3 Impacts of the GS front on moisture and storm tracks

As discussed above, the genesis of ARs is closely linked to water vapor supply and extratropical storm activities. The influence of the GS front on column-integrated water vapor (TMQ) and 300 hPa storm track ($V'V'$, V' is 5–12 day bandpass filtered data following Orlanski 2008) is further investigated and shown in Fig. 7. The GS front region is where the ocean provides intense water vapor into the atmosphere and is also the entrance of extratropical storm systems (Fig. 7a, b), creating preferential conditions for AR formation. The inclusion of the GS front in CTRL results in a significant TMQ increase along the GS front (Fig. 7d), supporting the higher AR occurrence and AR-IVT shown in Fig. 3. The net water vapor increase agrees with previous studies and is related to the non-linear water vapor response between warm and cold SST anomalies due to Clausius–Clapeyron relationship. The increased water vapor in the GS region then interacts with storms passing by. At the genesis stage of ARs, excessive water vapor is transported into the warm conveyor belt of extratropical storms. As storms travel, high water vapor

filaments are left behind and AR forms (Fig. 6; Dacre et al. 2019; Liu et al. 2021). After genesis, water vapor is transported further downstream following the propagation of ARs. When ARs reach Western Europe and make land-fall, water vapor is deposited around Iberian Peninsula, contributing to the intensification of TMQ downstream in CTRL (Fig. 7d).

The propagation of ARs is highly constrained by the storm trajectory. In response to the stronger GS front, there is a southward shift of upper-level storm track downstream in Western Europe (Fig. 7c), aligning closely with the downstream shift of ARs. The impact of mesoscale oceanic eddies and fronts on storm track response has been extensively discussed in previous studies (Ma et al. 2017; Foussard et al. 2019; Small et al. 2018). It has been argued that mesoscale SSTs primarily affect storm growth by modifying the moist diabatic processes and further changing the large-scale circulation through eddy-mean flow interaction. As discussed in the later section, we will show that the downstream shift of both ARs and storm tracks can be related to the modulation of Rossby wave train by the GS front.

3.4 Impacts of the GS front on vertical motion and heating

The AR composite analysis has provided insights into the significant enhancement of upward motion and diabatic heating associated with ARs when the GS front is included in CTRL from a Lagrangian perspective, indicating a potentially stronger heating effect exerted by frontal and mesoscale SST anomalies associated with the GS front. To investigate whether there is a fixed heating source associated with the GS front that could drive the stationary atmospheric Rossby wave response, the upward motion (W) and diabatic heating ($Q1$) response in CTRL and FLTR simulations are further compared from an Euler perspective.

Figure 8a, b, e, f below show the spatial distribution of upward motion and diabatic heating when ARs pass the GS region (referred to as AR days, comprising approximately 40% of the total winter season days) in CTRL, along with the corresponding differences between CTRL and FLTR. Two distinct regions of ascending motion are observed in the North Atlantic (Fig. 8a). One region is localized above the southern flank of the GS front, attributed to the underlying warm SST, while the other is situated along the coast of Western Europe, associated with topography lifting. The ascending motion transports moisture upward, resulting in precipitation and condensational heating within the atmospheric column. The corresponding heavy precipitation and strong diabatic heating in these regions are verified in Figs. 2h and 8b.

In comparison to FLTR, the presence of the GS front in CTRL induces an anomalous vertical circulation above the GS front, characterized by stronger ascending motion above the warm front and descending motion over the northern and southern flanks (Fig. 8e). The fractional change in vertical motion is approximately 20%. A similar anomalous circulation response to SST anomalies associated with the Kuroshio front was also reported by Xu et al. (2019). Additionally, the GS front tends to intensify the uplifting along the coast of western Europe (Fig. 8e), probably due to the strengthening of ARs in CTRL. In general, the heating response in the GS and the downstream coastal regions are consistent with the vertical motion response except that the fractional change of $Q1$ between CTRL and FLTR is higher, reaching ~30–50% (Fig. 8f). We also note a broad region of enhanced heating north of 50° N in CTRL. This heating exhibits a larger spatial scale than the heating in the GS region and becomes even stronger during non-AR days (Fig. 8d, h), implying coherent responses throughout the winter season. We speculate that the broad heating north of 50° N might be related to large-scale background circulation changes between CTRL and FLTR, rather than being related to ARs.

Figure 8c, d, g, h illustrate the upward motion and diabatic heating in CTRL and FLTR during non-AR days in the GS region. Compared to the results during AR days, the ascending motion above the GS front is almost absent (Fig. 8c). Correspondingly, the heating in the GS region is substantially reduced (Fig. 8d). These results exclude the impact of ARs and primarily reflect the influence of oceanic front forcing on the atmospheric mean state alone. It is evident that the significant ascending motion and heating observed above the GS front primarily occur during AR days, while the non-AR days component has limited contribution. This is consistent with previous studies that have emphasized the dominant role of atmospheric fronts in determining the time-mean air–sea coupling in western boundary current regions (Parfitt and Seo 2018; Sheldon et al. 2017). Although the smoothing of the GS front during non-AR days still induces changes in vertical motion (Fig. 8g), the heating change in the GS region weakens, and the downstream heating in the high topography area is attenuated compared to situations when ARs are present (Fig. 8h). A notable heating difference that appears during non-AR days is the existence of a large-scale heating pattern north of the GS forcing region, potentially associated with background circulation changes, as discussed earlier.

The contrasting atmospheric responses in the GS region with and without ARs are further illustrated by the vertical profiles of W and $Q1$ along 60° W (Fig. 9). With the occurrence of ARs, the ascending motion and heating above the GS front (around 40° N) extend up to 300 hPa (contours in Fig. 9a, c). In contrast, when ARs are absent, the ascending motion and heating are significantly weaker and largely confined below 600 hPa (contours in Fig. 9b, d). The average $Q1$ (700 hPa) without ARs is approximately 1/3 of the value with ARs, while w (700 hPa) without ARs is only 1/8 of that with ARs. Below PBL, the inclusion of the GS front induces a comparable enhancement of W in both cases (shading in Fig. 9a, b). However, the W response to the GS front during AR days extends much deeper than during non-AR days, leading to enhanced ascending motion above the PBL (shading in Fig. 9a). Correspondingly, the co-occurrence of the GS front and ARs also generates deeper and stronger heating compared to non-AR days (shading in Fig. 9c, d), with ARs amplifying the heating effect. The deep ascending motion above the PBL is crucial for precipitation formation and the release of heat at upper levels, facilitating the growth of ARs and cyclones (Ma et al. 2017; Foussard et al. 2019; Zhang et al. 2019a) and potentially influencing the atmospheric wave response.

Collectively, the comparison between AR days and non-AR days components demonstrates that the ascending and heating induced by the combined effect of AR and ocean front are notably deeper and stronger than those induced by the GS front only. The occurrence of ARs amplifies the

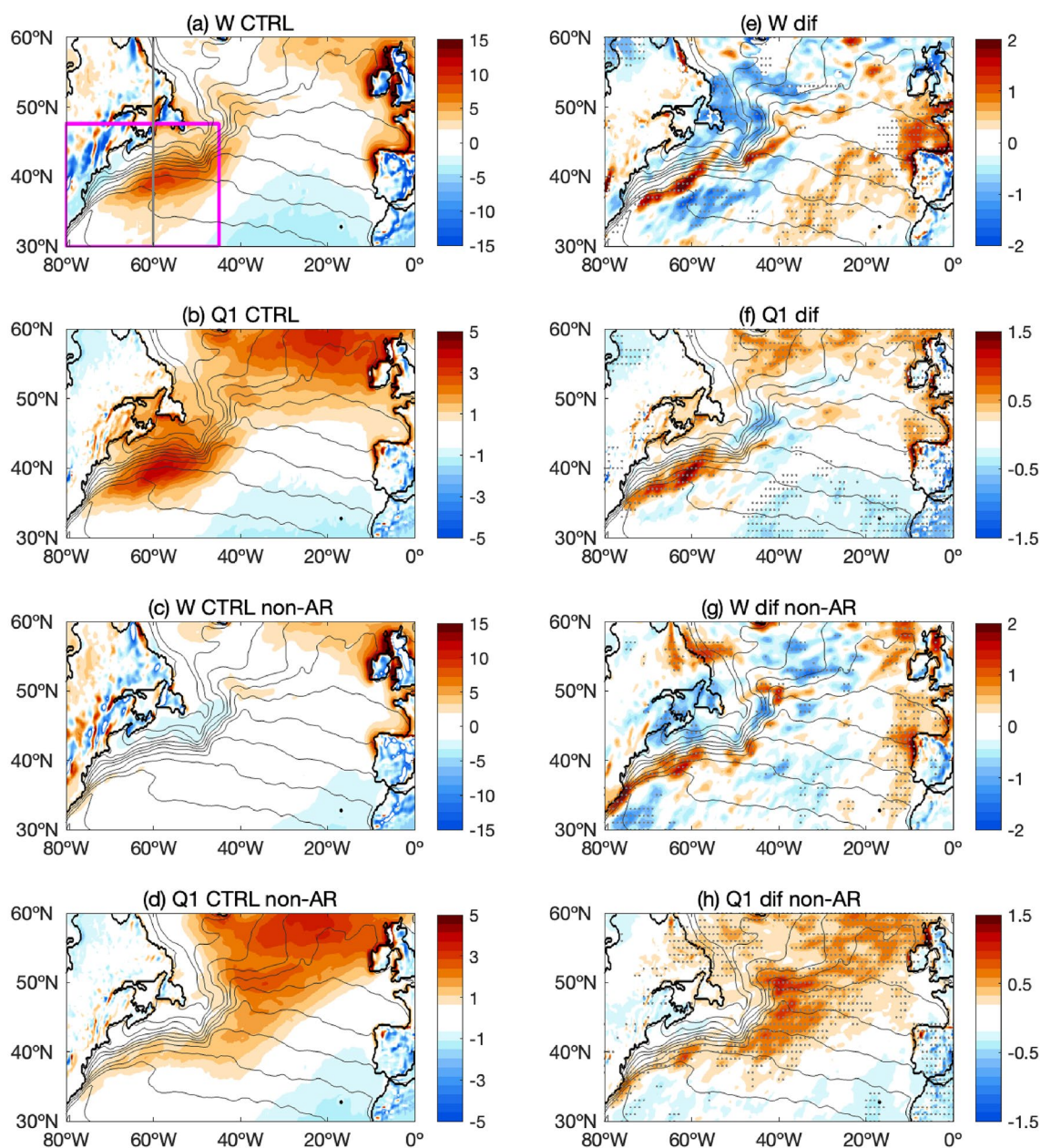


Fig. 8 Composites of vertical velocity (W , shading, $-10^{-2} \text{ Pa s}^{-1}$) (a) and apparent heating ($Q1$, shading, K day^{-1}) (b) at 700 hPa during AR days in CTRL and the corresponding differences between CTRL and FLTR (e, f). (c, d) are the same as (a, b), but for non-AR days composites. (g, h) are the same as (e, f), but for differences between CTRL and FLTR composited on non-AR days. Differences significant

above the 95% confidence level are shaded by grey dots based on a two-tailed Student's test. The magenta box outlines the GS region ($30^\circ \text{ N} - 47.5^\circ \text{ N}$, $80^\circ \text{ W} - 45^\circ \text{ W}$) used to define AR days. The grey line indicates the position of the vertical section plotted in Fig. 9 and Fig. 11

ocean–atmosphere interaction in the GS front region and is essential for the upward momentum and heat transfer associated with the underlying oceanic front, leading to a profound atmospheric response throughout the troposphere. The results confirm the amplification of synoptic weather systems in defining extratropical ocean–atmosphere

interaction in oceanic frontal regions, consistent with previous studies (Parfit and Seo 2018; Sheldon et al. 2017).

3.5 Impacts of the GS front on Rossby wave train

The above analyses have confirmed the existence of a fixed and intense heating source above the GS front, with up to a

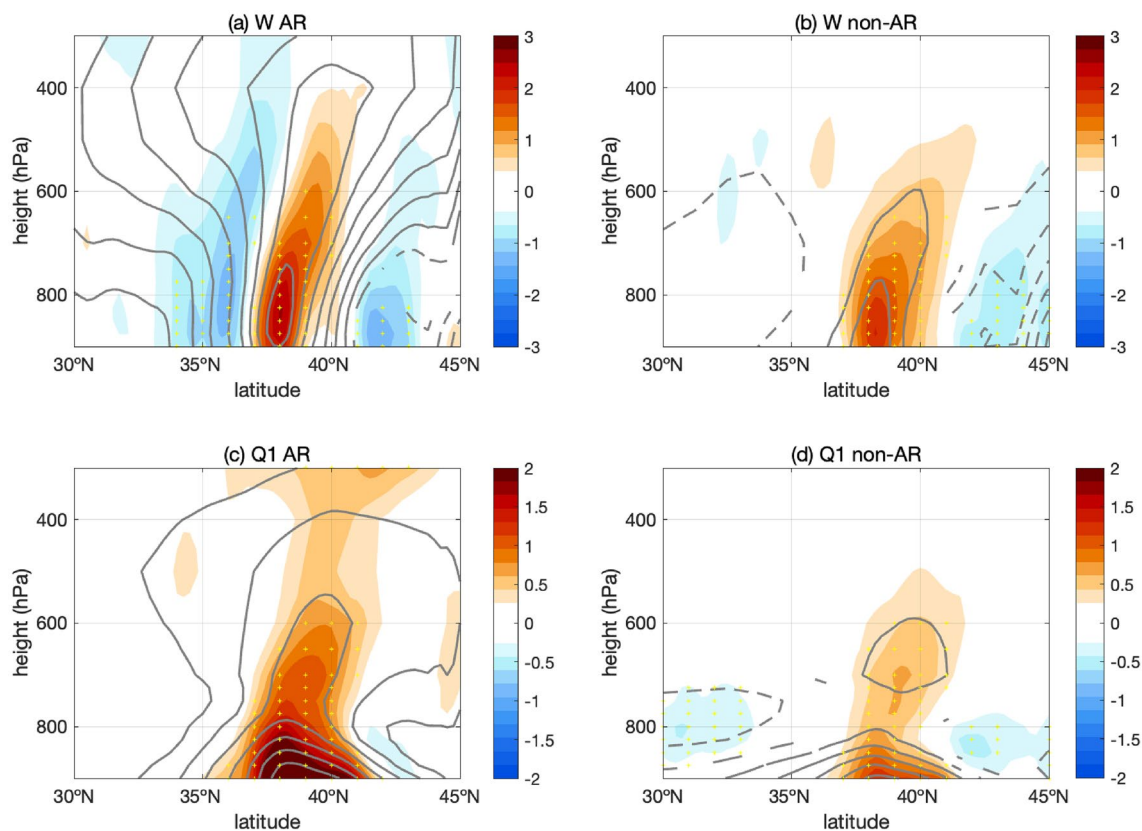


Fig. 9 Composites of the vertical cross-section of vertical velocity (W , $-10^{-2} \text{ Pa s}^{-1}$) (a) and apparent heating ($Q1$, K day^{-1}) (c) averaged between 65° W and 60° W during AR days in CTRL (contours) and the corresponding difference between CTRL and FLTR (shad-

ing). (b, d) are the same as (a, c), but for non-AR days composites. Differences significant above the 95% confidence level are shaded by stars based on a two-tailed Student's test

50% increase in heat in this region when the GS front is present. In accordance with the Rossby wave theory (Held et al. 2002; Wills et al. 2019), the strengthened diabatic heating in the atmospheric column may drive Rossby wave response and thereby influence the propagation of ARs in the North Atlantic. Figure 10 shows the 300 hPa geopotential height anomalies and wave activity flux (WAF) associated with AR days in CTRL, FLTR, and the corresponding differences between CTRL and FLTR. A distinct wave pattern emerges in the North Atlantic, characterized by high pressure anomalies above the GS front and northern Europe, and low pressure anomalies near the eastern US and Iceland (shading in Fig. 10a). Similar patterns with a weaker amplitude and a noticeable phase shift are observed in geopotential height anomalies at 850 hPa (red contours in Fig. 10a), suggesting the baroclinic nature of the wave. The high-pressure anomalies coincide with the most intense heating in the GS region (Fig. 8b). In fact, the heating above the GS front can reach values as high as 5 K/day , or even higher during AR days, which has been reported to be sufficient for triggering wave trains in the troposphere (An et al. 2022; Luo et al. 2022). The WAF exhibits a wave propagation from the GS region to

the Eurasian continent, with gradually decaying amplitude (vectors in Fig. 10a), and the propagation path generally follows the jet stream (green contours in Fig. 10a). A significant divergence of WAF is observed in the GS region, confirming the sourcing of the Rossby wave in the GS region (Takaya and Nakamura 2001).

A similar upstream Rossby wave structure is found in FLTR when the GS front is weakened, but the downstream Rossby wave is diminished (Fig. 10b). Moreover, the Rossby wave in FLTR tends to propagate over a shorter distance compared to CTRL, with distinct patterns confined to the Atlantic Ocean (Fig. 10b). The reduced downstream wave activity aligns with the decreased heating in the uplifting region when ARs make landfall in Western Europe (Fig. 8f). A closer examination of the geopotential height anomaly difference between CTRL and FLTR reveals south-north dipoles near the west of Europe and the Eurasian continent, characterized by strong high-pressure anomalies over the Eurasian continent. This indicates a shift in the south-north direction of the entire wave train according to geostrophy, consistent with the downstream response of ARs and storm tracks depicted in Figs. 3 and 7.

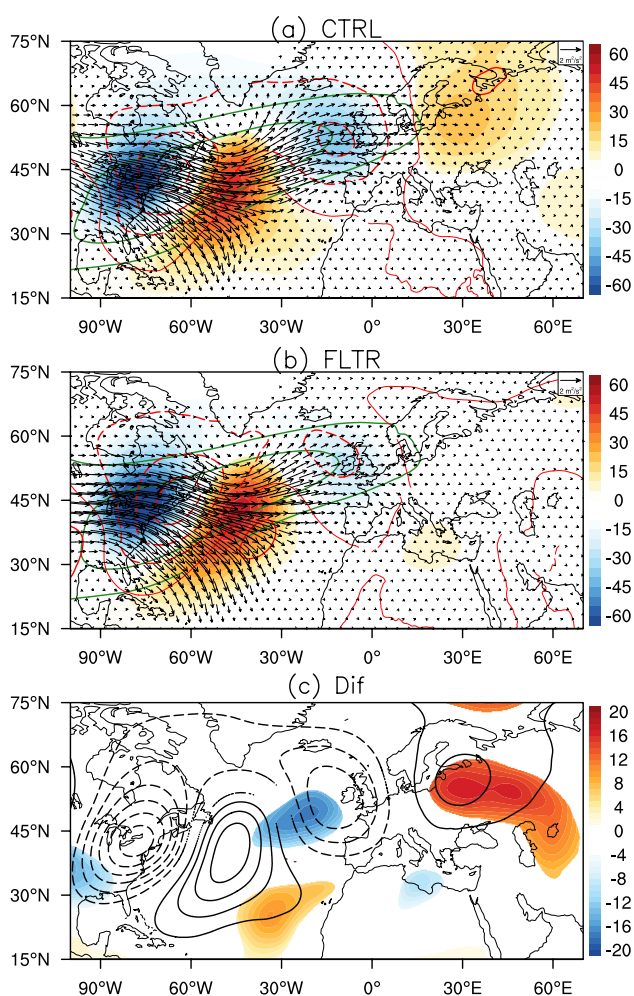


Fig. 10 Composites of geopotential height anomalies at 300 hPa (shading, m) and 850 hPa (red contours, the interval is 10 m, the thin contour is the zero line), wave activity flux (vectors, $\text{m}^2 \text{s}^{-2}$) and the zonal jet (green contours, m) at 300 hPa during AR days in CTRL (a) and FLTR (b). The composite difference of geopotential height anomalies between CTRL and FLTR (c, shading), differences significant above the 95% confidence level based on a Student's test are shown only. Black contours (the interval is 10 m, zero line did not shown) overlaid in c indicate the composite of geopotential height anomalies at 300 hPa in CTRL

The vertical propagation of the wave activity is further investigated. Figure 11 displays a cross-section plot of the vertical component of WAF in the GS region with and without ARs. During AR days, a robust upward propagation of WAF characterized by dual maxima near the surface and at the upper atmosphere is observed (Fig. 11a, b), confirming the characteristic structure of Rossby waves (Charney and Drazin 1961; Takaya and Nakamura 2001). A striking contrast is noted between AR and non-AR days, with non-AR days showing considerably weaker upward WAF (Fig. 11d, e). This once again highlights the crucial role of ARs in driving the deep ascending motion (heating) and the

upward propagation of WAF, which triggers upper troposphere Rossby wave response that further modulates the propagation of storms and ARs. Regarding the influence of GS front, the inclusion of the GS front in CTRL results in a slight intensification of upward WAF below 700 hPa, concentrated around the GS front (Fig. 11c). Meanwhile, a reduction of upward WAF is observed north of the front, in agreement with the ascending motion and heating observed above the GS front and descending motion to its north in Fig. 9. Moreover, the reduction in WAF north of the GS front also appears during non-AR days and is more pronounced, implying its potential linkage to atmospheric mean state (Fig. 11f). The results indicate that while the presence of GS front exerts a discernible effect on vertical WAF, its overall influence remains relatively modest.

4 Conclusions and discussions

In this study, we investigated the influence of SST anomalies associated with the GS front on ARs in the North Atlantic by comparing two sets of multi-ensemble global CAM simulations with (CTRL) and without (FLTR) the GS front in the boreal winter season (DJF). Our findings indicate that the inclusion of the GS front in CTRL results in approximately 25% enhancement of AR-IVT and AR-induced precipitation in the GS region. Moreover, this inclusion leads to a more notable response of ARs downstream in Western Europe, with up to 60% precipitation increases observed around Spain and precipitation reductions of up to 40% around Norway for the most extreme events (exceeding 90 mm/day). The AR composite analysis suggests an overall intensification of ARs with the presence of the GS front. Compared to FLTR, ARs in CTRL are associated with deeper SLP anomalies, enhanced water vapor transport, stronger upward motion and diabatic heating.

The thermodynamic and dynamic factors through which the GS front may exert influence on ARs are further explored. Thermodynamically, the inclusion of the GS front brings increased water vapor in both the GS region and Western Europe, creating favorable conditions for AR genesis. Dynamically, the presence of the GS front in CTRL corresponds to a shift of storm track and modulation of the Rossby wave train, contributing to the southward shift of downstream ARs in Western Europe. Furthermore, the dynamic process is closely linked to the thermodynamic process. Particularly, when ARs pass by the GS region, deep ascending and heating develop above the GS front, which is crucial for perturbing the deep troposphere and triggering upper level Rossby wave response. The amplified ocean–atmosphere interaction by the synoptic ARs is the key driving the aforementioned deep troposphere response.

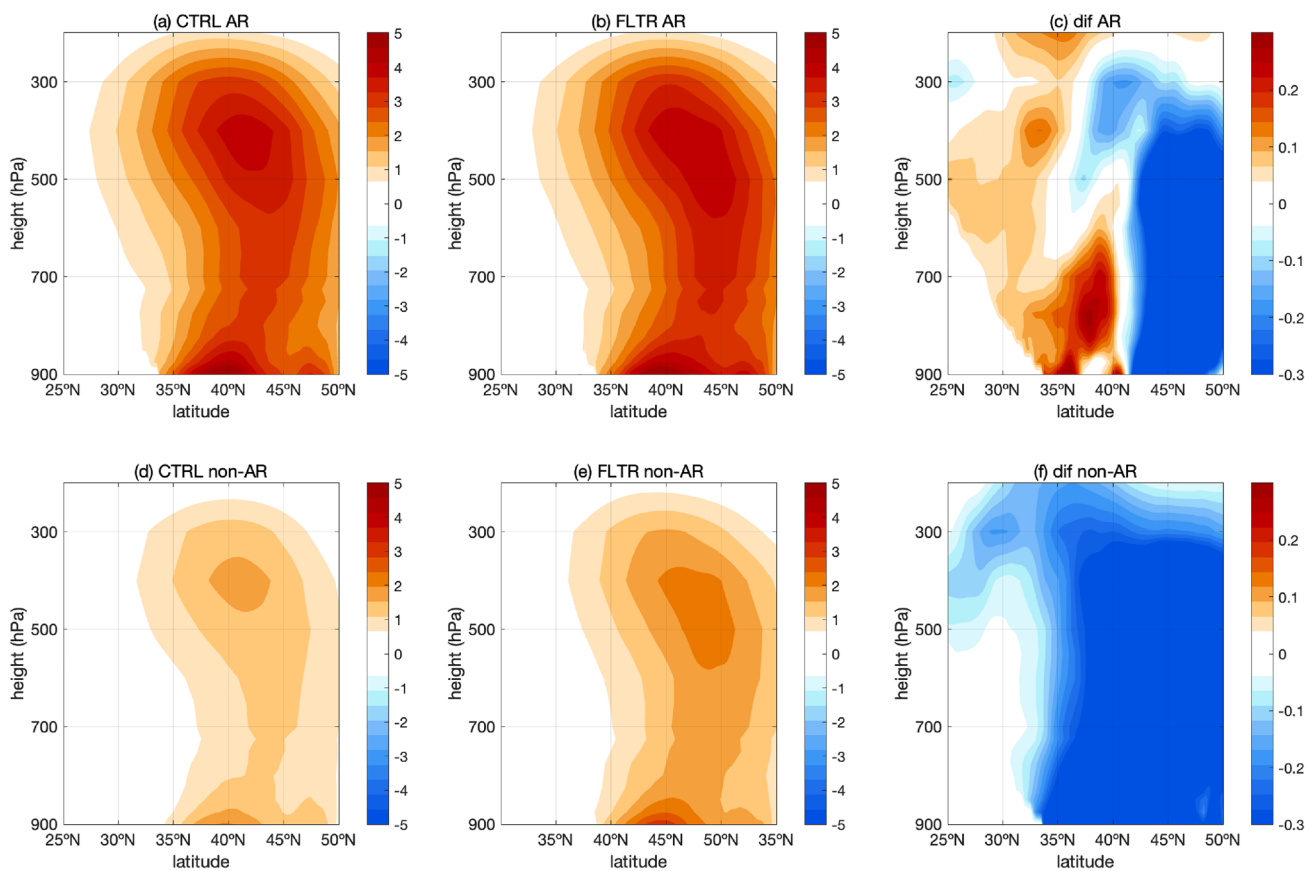


Fig. 11 Composites of the vertical cross-section of vertical wave activity flux component (positive value denotes upward propagation. Unit: $10^{-2} \text{ Pa m s}^{-2}$) averaged between 65° W and 60° W during AR days in CTRL (**a**), FLTR (**b**) and the difference between CTRL and

FLTR (**c**). (**d–f**) are the same as (**a–c**), but for non-AR days composites. Note that the wave activity flux is calculated where the zonal velocity in the mean state is larger than 5 m s^{-1}

The impacts of frontal and mesoscale SST forcing on storm tracks and precipitation in the Kuroshio and GS regions have been investigated by many previous studies (see Czaja et al. 2019; Seo et al. 2023 for reviews). In our study, we specifically focused on the influence of the GS front on ARs, which play a crucial role in producing extreme precipitation. The enhanced ARs in the GS region and the shift of the downstream ARs at the presence of the GS front agree with previous studies investigating storm tracks and atmospheric circulation responses in both the Kuroshio and the GS region (Ma et al. 2015, 2017; Kuwano-Yoshida and Minobe 2017; Sheldon et al. 2017; Small et al. 2018), confirming the robustness of the frontal and mesoscale SSTs in affecting the extratropical weather systems. Nevertheless, discrepancies exist in the reported shifting of ARs and storm tracks in response to the GS front, which may be attributed to different model resolutions and the background atmospheric circulation state as suggested by previous research (Peng et al. 1997; Czaja et al. 2019). Another notable difference is that

our findings revealed that the inclusion of the GS front brings significant and even stronger AR and precipitation responses in remote areas than that in the GS region, while previous studies have suggested ambiguous or generally weaker atmospheric responses remotely. The results seem to suggest that ARs are more responsive to oceanic front and eddy forcing than storm tracks, implying that when incorporating the influence of frontal and mesoscale oceanic processes in numerical simulations, ARs may offer improved sub-seasonal to seasonal prediction skills compared to extratropical storms and in-depth study associated with this problem is planned in the future.

Acknowledgements We thank the National Supercomputing Center in Tianjin and Jinan for providing the computing resources that contributed to the research in this paper.

Author contributions All authors contributed the study conception and design. Material preparation, data collection and analysis were performed by JYL and HZQ. JYL prepared the figures, JYL first drafted the manuscript, MXH improved the writing and provided interpretations of the results, all authors read and approved the final manuscript.

Funding This research is supported by the National Natural Science Foundation of China (42376025, 41975065), the Science and Technology Innovation Program of Laoshan Laboratory (LSKJ202300302, LSKJ202202503), Shandong Provincial Natural Science Foundation (ZR2022YQ29, ZR2019ZD12), Taishan Scholar Funds (tsqn202103028) and Taishan Panddeng Scholar Project.

Data availability The CAM5 Model output analyzed in this study are available from the corresponding author on reasonable request. The ERA5 data is available at <https://cds.climate.copernicus.eu/cdsapp#!/dataset>. The OISST data is available at <https://climatedataguide.ucar.edu/climate-data/sst-data-noaa-high-resolution-025x025-blended-analysis-daily-sst-and-ice-oisstv2>.

Declarations

Conflict of interest The authors declare that there were no business or financial relationships that may be seen as having a conflict of interest throughout the course of the research.

Open Access This article is licensed under a Creative Commons Attribution 4.0 International License, which permits use, sharing, adaptation, distribution and reproduction in any medium or format, as long as you give appropriate credit to the original author(s) and the source, provide a link to the Creative Commons licence, and indicate if changes were made. The images or other third party material in this article are included in the article's Creative Commons licence, unless indicated otherwise in a credit line to the material. If material is not included in the article's Creative Commons licence and your intended use is not permitted by statutory regulation or exceeds the permitted use, you will need to obtain permission directly from the copyright holder. To view a copy of this licence, visit <http://creativecommons.org/licenses/by/4.0/>.

References

- An X, Sheng L, Li C et al (2022) Effect of rainfall-induced diabatic heating over southern China on the formation of wintertime haze on the North China Plain. *Atmos Chem Phys* 22:725–738. <https://doi.org/10.5194/acp-22-725-2022>
- Arabzadeh A, Ehsani MR, Guan B et al (2020) Global intercomparison of atmospheric rivers precipitation in remote sensing and reanalysis products. *J Geophys Res*. <https://doi.org/10.1029/2020JD033021>
- Bui H, Spengler T (2021) On the influence of sea surface temperature distributions on the development of extratropical cyclones. *J Atmos Sci* 78:1173–1188. <https://doi.org/10.1175/JAS-D-20-0137.1>
- Charney JG, Drazin PG (1961) Propagation of planetary-scale disturbances from the lower into the upper atmosphere. *J Geophys Res* 66(1):83–109. <https://doi.org/10.1029/JZ066i001p00083>
- Czaja A, Frankignoul C, Minobe S et al (2019) Simulating the mid-latitude atmospheric circulation: what might we gain from high-resolution modeling of air-sea interactions? *Curr Clim Change Rep* 5:390–406. <https://doi.org/10.1007/s40641-019-00148-5>
- Dacre HF, Clark PA, Martínez-Alvarado O et al (2015) How do atmospheric rivers form? *Bull Am Meteorol Soc* 96:1243–1255. <https://doi.org/10.1175/BAMS-D-14-00031.1>
- Dacre HF, Martínez-Alvarado O, Mbengue CO (2019) Linking atmospheric rivers and warm conveyor belt airflows. *J Hydrometeorol* 20:1183–1196. <https://doi.org/10.1175/JHM-D-18-0175.1>
- de Vries AJ (2021) A global climatological perspective on the importance of Rossby wave breaking and intense moisture transport for extreme precipitation events. *Weather Clim Dyn* 2:129–161. <https://doi.org/10.5194/wcd-2-129-2021>
- Foussard A, Lapeyre G, Plougonven R (2019) Storm track response to oceanic eddies in idealized atmospheric simulations. *J Clim* 32:445–463. <https://doi.org/10.1175/JCLI-D-18-0415.1>
- Gimeno L, Nieto R, Vázquez M et al (2014) Atmospheric rivers: a mini-review. *Front Earth Sci* 2:1–6. <https://doi.org/10.3389/feart.2014.00002>
- Graff LS, LaCasce JH (2012) Changes in the extratropical storm tracks in response to changes in SST in an AGCM. *J Clim* 25:1854–1870. <https://doi.org/10.1175/JCLI-D-11-00174.1>
- Guan B, Waliser DE (2015) Detection of atmospheric rivers: evaluation and application of an algorithm for global studies. *J Geophys Res Atmos* 120:12514–12535. <https://doi.org/10.1002/2015JD024257>
- Held IM, Ting M, Wang H (2002) Northern winter stationary waves: theory and modeling. *J Clim* 15:2125–2144. [https://doi.org/10.1175/15200442\(2002\)015%3c2125:NWSWTA%3e2.0.CO;2](https://doi.org/10.1175/15200442(2002)015%3c2125:NWSWTA%3e2.0.CO;2)
- Hsu H-H, Chen Y-T (2020) Simulation and projection of circulations associated with atmospheric rivers along the North American northeast coast. *J Clim* 33:5673–5695. <https://doi.org/10.1175/JCLI-D-19-0104.1>
- Kuwano-Yoshida A, Minobe S (2017) Storm-track response to SST fronts in the northwestern Pacific region in an AGCM. *J Clim* 30:1081–1102. <https://doi.org/10.1175/JCLI-D-16-0331.1>
- Kwon Y-O, Alexander MA, Bond NA et al (2010) Role of the Gulf Stream and Kuroshio-Oyashio systems in large-scale atmosphere-ocean interaction: a review. *J Clim* 23:3249–3281. <https://doi.org/10.1175/2010JCLI3343.1>
- Lavers DA, Villarini G (2013) The nexus between atmospheric rivers and extreme precipitation across Europe. *Geophys Res Lett* 40:3259–3264. <https://doi.org/10.1002/grl.50636>
- Lee RW, Woollings TJ, Hoskins BJ et al (2018) Impact of Gulf Stream SST biases on the global atmospheric circulation. *Clim Dyn* 51:3369–3387. <https://doi.org/10.1007/s00382-018-4083-9>
- Liu X, Ma X, Chang P et al (2021) Ocean fronts and eddies force atmospheric rivers and heavy precipitation in western North America. *Nat Commun* 12:1268. <https://doi.org/10.1038/s41467-021-21504-w>
- Luo Y, Shi J, An X et al (2022) The combined impact of subtropical wave train and Polar–Eurasian teleconnection on the extreme cold event over North China in January 2021. *Clim Dyn* 60:3339–3352. <https://doi.org/10.1007/s00382-022-06520-w>
- Ma X, Chang P, Saravanan R et al (2015) Distant influence of Kuroshio eddies on north Pacific weather patterns. *Sci Rep* 5:17785. <https://doi.org/10.1038/srep17785>
- Ma X, Chang P, Saravanan R et al (2017) Importance of resolving Kuroshio front and eddy influence in simulating the north Pacific storm track. *J Clim* 30:1861–1880. <https://doi.org/10.1175/JCLI-D-16-0154.1>
- McClenny EE, Ullrich PA, Grotjahn R (2020) Sensitivity of atmospheric river vapor transport and precipitation to uniform sea surface temperature increases. *J Geophys Res Atmos* 125:e2020JD033421. <https://doi.org/10.1029/2020JD033421>
- Minobe S, Kuwano-Yoshida A, Komori N et al (2008) Influence of the Gulf Stream on the troposphere. *Nature* 452:206–209. <https://doi.org/10.1038/nature06690>
- Minobe S, Miyashita M, Kuwano-Yoshida A et al (2010) Atmospheric response to the Gulf Stream: seasonal variations. *J Clim* 23:3699–3719. <https://doi.org/10.1175/2010JCLI3359.1>
- O'Reilly CH, Minobe S, Kuwano-Yoshida A et al (2017) The Gulf Stream influence on wintertime North Atlantic jet variability. *Q J R Meteorol Soc* 143:173–183. <https://doi.org/10.1002/qj.2907>
- Orlanski I (2008) The rationale for why climate models should adequately resolve the mesoscale. In: Hamilton K, Ohfuchi W (eds) High resolution numerical modelling of the atmosphere and

- ocean. Springer, New York, pp 29–44. https://doi.org/10.1007/978-0-387-49791-4_2
- Parfitt R, Seo H (2018) A new framework for near-surface wind convergence over the Kuroshio Extension and Gulf Stream in winter-time: the role of atmospheric fronts. *Geophys Res Lett* 45:9909–9918. <https://doi.org/10.1029/2018GL080135>
- Parfitt R, Czaja A, Minobe S et al (2016) The atmospheric frontal response to SST perturbations in the Gulf Stream region. *Geophys Res Lett* 43:2299–2306. <https://doi.org/10.1002/2016GL067723>
- Peng S, Robinson WA, Hoerling MP (1997) The modeled atmospheric response to midlatitude SST anomalies and its dependence on background circulation states. *J Clim* 10(5):971–987. [https://doi.org/10.1175/1520-0442\(1997\)010%3c0971:TMARTM%3e2.0.CO;2](https://doi.org/10.1175/1520-0442(1997)010%3c0971:TMARTM%3e2.0.CO;2)
- Piazza M, Terray L, Boé J et al (2016) Influence of small-scale North Atlantic sea surface temperature patterns on the marine boundary layer and free troposphere: a study using the atmospheric ARPEGE model. *Clim Dyn* 46:1699–1717. <https://doi.org/10.1007/s00382-015-2669-z>
- Seo H, O'Neill LW, Bourassa MA et al (2023) Ocean mesoscale and frontal-scale ocean–atmosphere interactions and influence on large-scale climate: a review. *J Clim* 36(7):1981–2013. <https://doi.org/10.1175/jcli-d-21-0982.1>
- Sheldon L, Czaja A, Vannièrè B et al (2017) A ‘warm path’ for Gulf Stream–troposphere interactions. *Tellus A* 69:1299397. <https://doi.org/10.1080/16000870.2017.1299397>
- Small RJ, deSzoeko SP, Xie SP et al (2008) Air–sea interaction over ocean fronts and eddies. *Dyn Atmos Oceans* 45(3–4):274–319. <https://doi.org/10.1016/j.dynatmoce.2008.01.001>
- Small RJ, Msadek R, Kwon Y-O et al (2018) Atmosphere surface storm track response to resolved ocean mesoscale in two sets of global climate model experiments. *Clim Dyn* 52:2067–2089. <https://doi.org/10.1007/s00382-018-4237-9>
- Sugimoto S, Aono K, Fukui S (2017) Local atmospheric response to warm mesoscale ocean eddies in the Kuroshio–Oyashio Confluence region. *Sci Rep* 7:11871. <https://doi.org/10.1038/s41598-017-12206-9>
- Takaya K, Nakamura H (2001) A formulation of a phase-independent wave-activity flux for stationary and migratory quasigeostrophic eddies on a zonally varying basic flow. *J Atmos Sci* 58:608–627. [https://doi.org/10.1175/1520-0469\(2001\)058%3c0608:AFOAPI%3e2.0.CO;2](https://doi.org/10.1175/1520-0469(2001)058%3c0608:AFOAPI%3e2.0.CO;2)
- Tsopouridis L, Spengler T, Spensberger C (2021) Smoother versus sharper Gulf Stream and Kuroshio sea surface temperature fronts: effects on cyclones and climatology. *Weather Clim Dyn* 2:953–970. <https://doi.org/10.5194/wcd-2-953-2021>
- Willison J, Robinson WA, Lackmann GM (2013) The importance of resolving mesoscale latent heating in the North Atlantic storm track. *J Atmos Sci* 70:2234–2250. <https://doi.org/10.1175/JAS-D-12-0226.1>
- Wills RCJ, White RH, Levine XJ (2019) Northern Hemisphere stationary waves in a changing climate. *Curr Clim Change Rep* 5:372–389. <https://doi.org/10.1007/s40641-019-00147-6>
- Wu Y, Jia Y, Ji R et al (2020) SST warming in recent decades in the Gulf Stream extension region and its impact on atmospheric rivers. *Atmosphere* 11:1109. <https://doi.org/10.3390/atmos11101109>
- Xu G, Chang P, Ma X et al (2019) Suppression of winter heavy precipitation in Southeastern China by the Kuroshio warm current. *Clim Dyn* 53:2437–2450. <https://doi.org/10.1007/s00382-019-04873-3>
- Yanai M, Esbensen S, Chu J-H (1973) Determination of bulk properties of tropical cloud clusters from large-scale heat and moisture budgets. *J Atmos Sci* 30:611–627. [https://doi.org/10.1175/1520-0469\(1973\)030%3c0611:DOBPOT%3e2.0.CO;2](https://doi.org/10.1175/1520-0469(1973)030%3c0611:DOBPOT%3e2.0.CO;2)
- Zavadoff BL, Kirtman BP (2020) Dynamic and thermodynamic modulators of European atmospheric rivers. *J Clim* 33:4167–4185. <https://doi.org/10.1175/JCLI-D-19-0601.1>
- Zhang Z, Ralph FM, Zheng M (2019a) The relationship between extratropical cyclone strength and atmospheric river intensity and position. *Geophys Res Lett* 46:1814–1823. <https://doi.org/10.1029/2018GL079071>
- Zhang X, Ma X, Wu L (2019b) Effect of mesoscale oceanic eddies on extratropical cyclogenesis: a tracking approach. *J Geophys Res Atmos* 124(12):6411–6422. <https://doi.org/10.1029/2019JD030595>
- Zhu Y, Newell RE (1998) A proposed algorithm for moisture fluxes from atmospheric rivers. *Mon Weather Rev* 126:725–735. [https://doi.org/10.1175/1520-0493\(1998\)126%3c0725:APAFMF%3e2.0.CO;2](https://doi.org/10.1175/1520-0493(1998)126%3c0725:APAFMF%3e2.0.CO;2)

Publisher's Note Springer Nature remains neutral with regard to jurisdictional claims in published maps and institutional affiliations.